SUPPLEMENTARY MATERIAL

3D-Printed Ceramic Membranes: Fabrication and Hydrogen Permeation Performance

A. Bartoletti[1,2], E. Mercadelli[1]*, V. Saraceni[3,4], A. Sangiorgi[1], A. Gondolini[1], C. Melandri[1], P. Pinasco[1], P. Gramazio[3], A. Fasolini[3,4], J. De Maron[3,4]*, F. Basile[3,5], A. Sanson[1]

[1] National Research Council of Italy, Institute of Science, Technology and Sustainability for Ceramics (CNR-ISSMC), Via Granarolo 64, 48018, Faenza, Italy

[2] Department of Chemical Sciences, Università degli Studi di Padova, Via Marzolo 1, 35131, Padova, Italy

[3] Department of Industrial Chemistry "Toso Montanari" University of Bologna, Viale Del Risorgimento 4, 40136, Bologna, Italy

[4] Center for Chemical Catalysis - C3, University of Bologna, Viale Del Risorgimento 4, 40136, Bologna, Italy

[5] Consorzio Interuniversitario per La Scienza e Tecnologia Dei Materiali (INSTM), Via G. Giusti, 9 50121, Firenze, Italy

Corresponding Authors

Elisa Mercadelli, elisa.mercadelli@cnr.it

Jacopo De Maron, jacopo.demaron2@unibo.it

Figure S1: Schematic representation of the developed process to obtain BCZY-GDC-based ceramics part by microextrusion

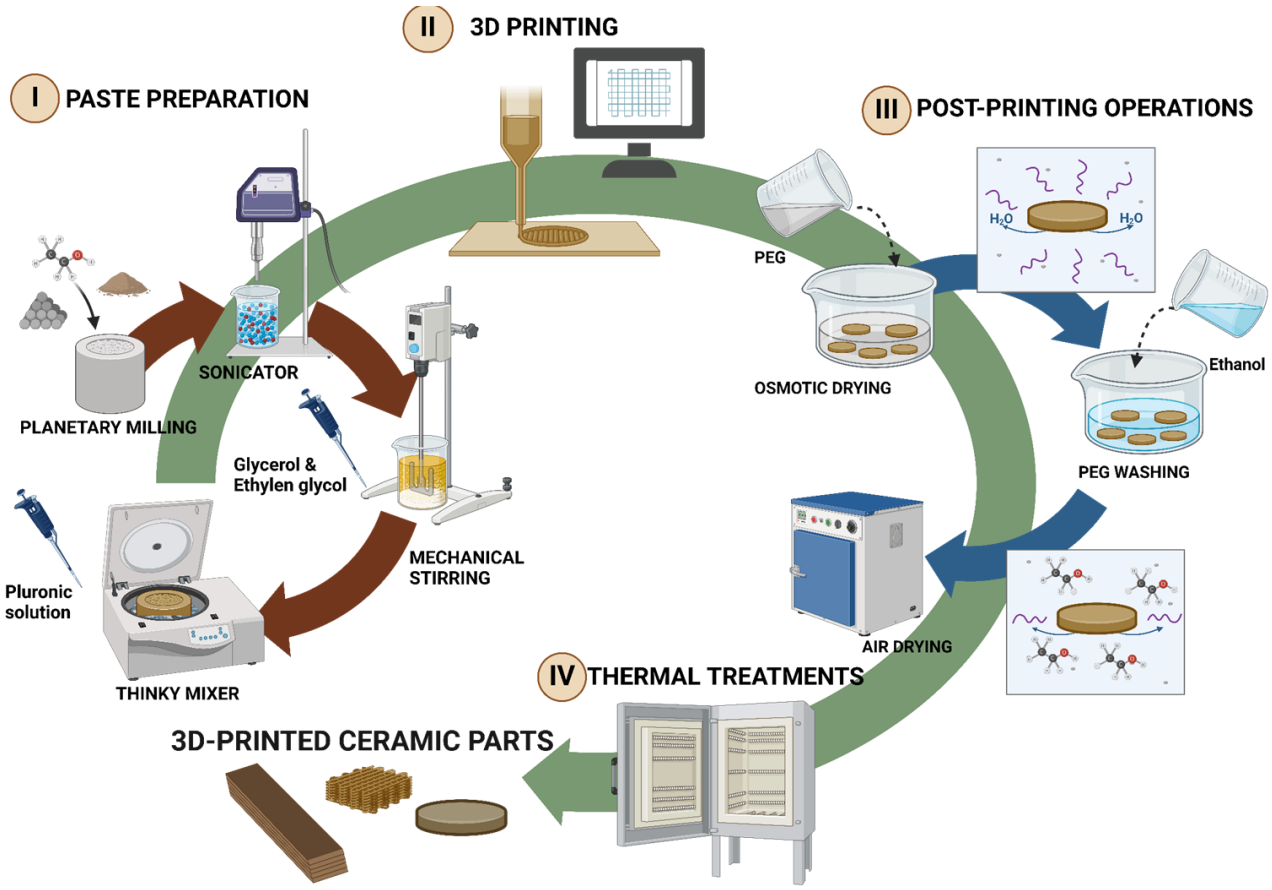

Figure S 1. Schematic representation of the developed process to obtain BCZY-GDC-based ceramic parts by microextrusion. Created in BioRender. Bartoletti, A. (2025) https://BioRender.com/r85u303.

Section S2: Production and characterization of BCZY-GDC specimens by dry-pressing

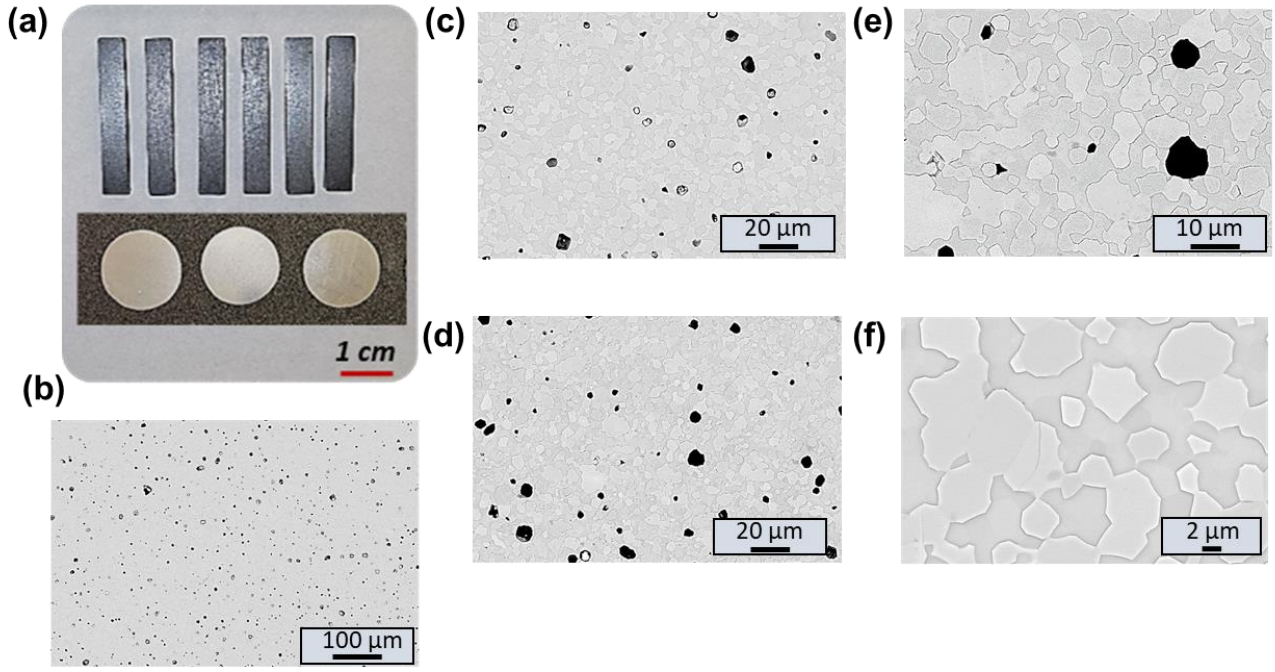

Figure S 2. Macroscopic picture of the as-produced membranes and test bars by dry-pressing (a) and SEM micrographs with BSE detector of a polished cross-section of sintered specimens at different magnifications (b-f). Here, lighter grains are associated with the GDC phase, the darker "matrix" is composed of BCZY, and black zones are pores. The sintered parts are characterized by a homogeneous microstructure (Figure S2 b-f) composed by large grains of 11.0 ± 2.9 µm and randomly distributed pores of 5.5 ± 2.2 µm. The total porosity calculated by image analysis is 2.8 ± 0.5 %, comparable to the one calculated using the Archimede's method.

Figure S3: X-Ray powder diffraction analysis of the starting ceramic powders

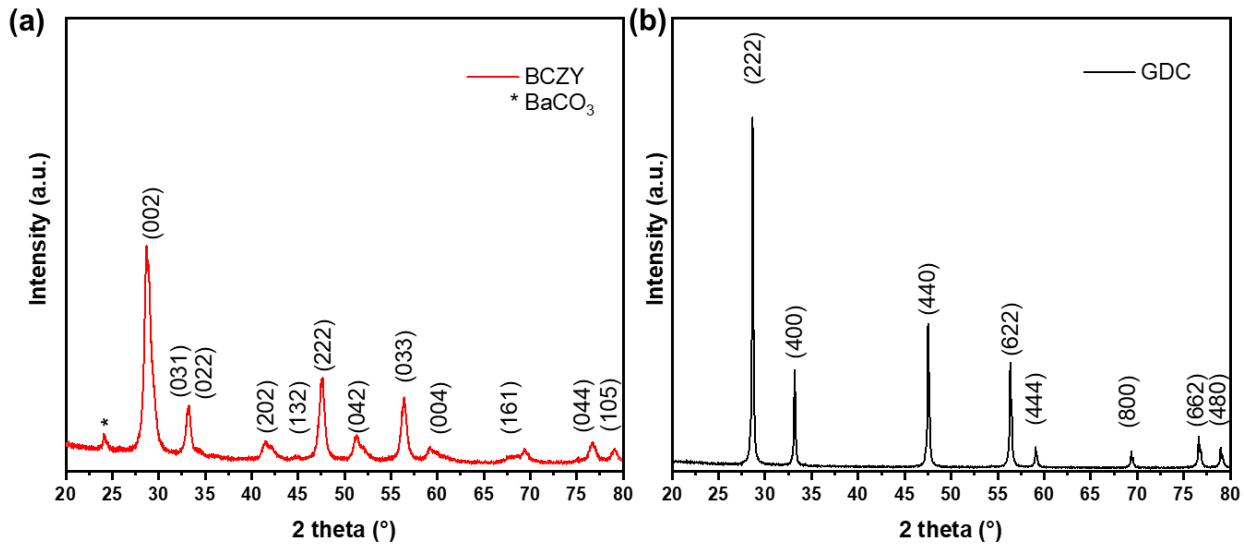

Figure S 3. XRPD of the starting ceramic powders: $BaCe_{0.65}Zr_{0.20}Y_{0.15}O_{3-\delta}$ (a) and $Ce_{0.8}Gd_{0.2}O_{2-\delta}$ (b).

Section S4: 3 Interval Thixotropy Test (3ITT) on the microextrusion ink and Thermal analysis of the Pluronic F-127 stock solution

The transition from fluid-like to solid-like behavior was investigated using the 3-Interval Thixotropy Test (3ITT) to assess the rheological recovery of the ink after printing. Viscosity recovery over time was measured following the removal of a high shear stress. The test was conducted at 25 °C using a rotational rheometer with controlled shear stress (C-VOR 120, Bohlin, Malvern Instruments, UK), equipped with a parallel plate geometry (1 mm gap) and a 20 mm diameter top plate (PP20). A solvent trap was employed to prevent water evaporation during the measurement.

The protocol consisted of three intervals: initially, a low shear rate of 0.01 s^{-1} was applied for 120 s to simulate the ink at rest in the tank; subsequently, a high shear rate of 100 s^{-1} was applied for 120 s to mimic the extrusion process; finally, the shear rate was reduced back to 0.01 s^{-1} for 120 s to reproduce post-printing rest conditions. The results, shown in Figure S4a, reveal stable viscosity values around ~6 × 10^4 Pa·s during the initial rest phase. Upon applying the high shear rate, viscosity rapidly dropped to ~100 Pa·s, indicating shear-thinning behavior. Remarkably, the ink exhibited full recovery within seconds once the shear rate was reduced, demonstrating excellent thixotropic recovery and ensuring good shape retention of the printed structures.

To better understand the thermal behaviour of the as-produced microextrusion paste, TG/DSC analysis was conducted on the 25 wt.% Pluronic aqueous solution as explained in the experimental section. These analyses were performed since, to the best of our knowledge, there is a lack in the literature regarding the thermal behaviour of concentrated Pluronic F-127 hydrogels. A deep understanding of the thermal behaviour of the as-produced ink is of pivotal importance to properly tune thermal treatments like debonding and sintering. Results are reported in **Figure S4 b**.

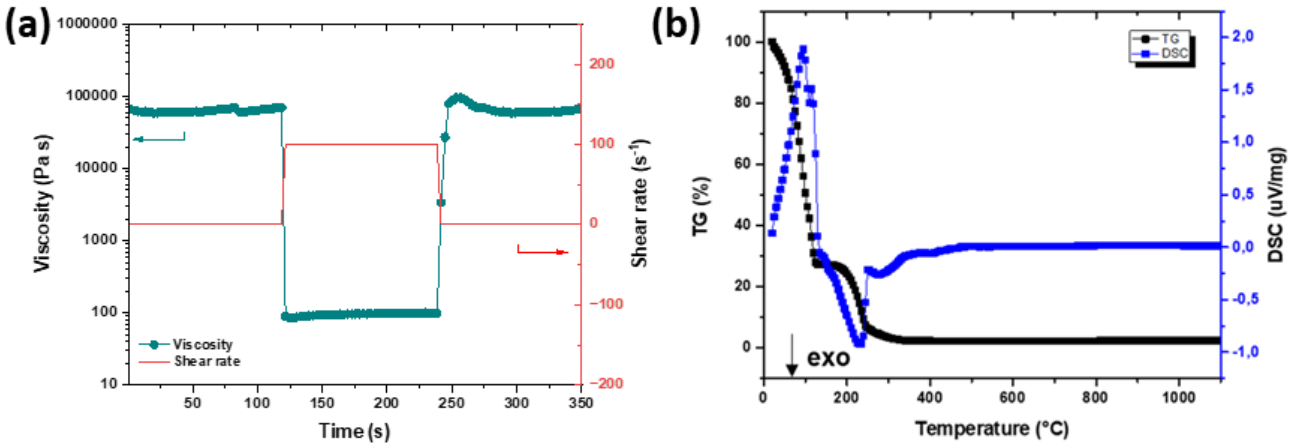

Figure S 4. 3ITT measurement performed on the microextrusion ink (a); TG/DSC analysis conducted on the Pluronic F-127 aqueous solution in air (b).

The thermogram shows the evaporation of water (75 wt. %) accompanied by a strong endothermic peak centred at 100°C and proceeds with the combustion of the polymeric system which finishes at 450 °C. In the end, 2% of the mass residue is present and associated with carbon coke. Observing the DSC curve it's possible to appreciate that the polymer decomposes through a multi-step reaction since Pluronic is a terpolymer constituted by polyethylene oxide (PEO) – polypropylene oxide (PPO) – PEO blocks. DSC curve is characterized by a first strong exothermic peak centred at 229 °C associated with the breakdown of PPO chains [1], followed by two less intense exothermic events centred at 280 °C and 410 °C, related to the degradation of PEO [2].

Figure S5: Sketches during 3D printing using different types of nozzles.

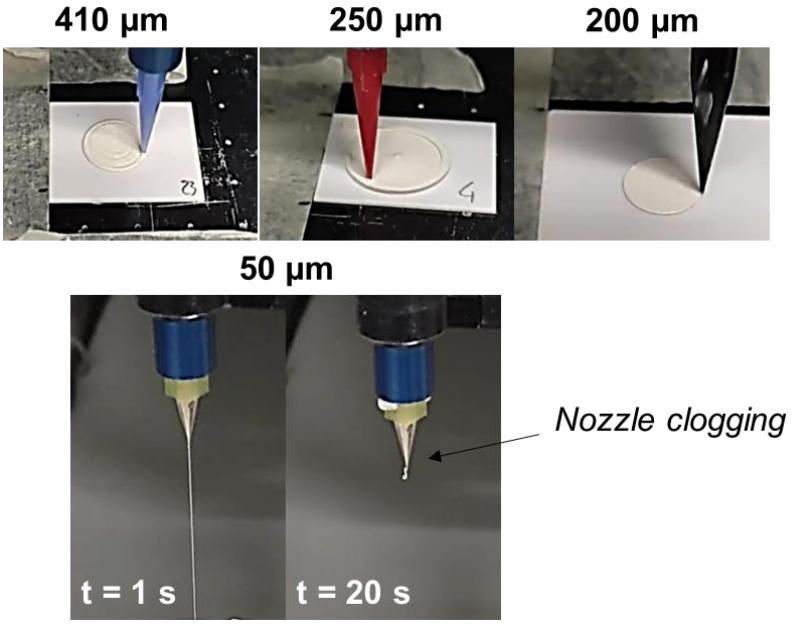

Figure S 5. Pics of different nozzles used in this study. QuantX Single Tapered Dispense Tips (410, 250, and 200 µm orifice sizes) and metallic QuantXTM Micron-S Precision dispense tip with 50 µm orifice size were employed. All these nozzles were purchased from Fisnar (USA).

Section S6: Productivity of the microextrusion process vs dry-pressing for green membrane manufacturing

The production of button membranes of about 15 mm in diameter involves the manufacturing of green ceramic parts ≈ Ø = 20 mm (surface area of ≈ 314 mm^2) considering the large shrinkage associated with the densification estimated to be ≈ 20-25% [3].

In traditional manufacturing techniques such as dry-pressing, being a batch process, the time to obtain the ceramic part at the Lab-scale is related to weighing the powder, filling the die, and pressing (without considering that all these factors strictly depend on the skill of the operator). In our laboratory, using the procedure described in the experimental section we estimate that the production of a green body by dry-pressing requires ≈ 6 minutes, therefore about 10 specimens per hour can be produced. In contrast, additive manufacturing (AM) techniques such as microextrusion involve the deposition of a suitable paste in a controlled pattern, therefore the time required to obtain a specimen is directly related to the dimension of the desired object.

As shown in **Table S1** the productivity in terms of part per hour for the manufacturing of button membranes can be increased by a factor > 5 through the developed set-up for microextrusion (depending on the printing speed) compared to dry-pressing. However, when considering the production of larger parts (e.g. discs of 65 mm diameter, surface area of ≈ 3318 mm^2) printing parameters have to be carefully evaluated to be competitive with other manufacturing techniques, especially the printing rate.

Table S1. Productivity in terms of (green) parts produced per hour for microextrusion and dry-pressing techniques used in this study.

Set up	Printing speed (ml/min)	Parts/h (Φ 20 mm)	Parts/h (Φ 65 mm)
1	5	57	5.5
2	10	114	11
3	40	456	44
Dry-pressing	/	10	10

It's worth mentioning that the comparison done here doesn't take into account the whole manufacturing process and the specific features of AM technology, such as the possibility of producing complex designs and thin parts which are difficult or almost impossible to obtain by dry-pressing. This comparison aims to point out that the choice of the printing parameters has an impact not only on the quality/dimension of the printed part but also on the production rate and hence the manufacturing cost [4], therefore manufacturers should consider them properly when approaching AM techniques such as direct ink writing (DIW).

Section S7: Possibility to reprint with the microextruded paste from scraps.

One of the multiple advantages of direct ink writing (DIW) is the possibility to minimize wastes related to specimen manufacturing since no supporting materials are required (also for complex geometries) and ceramic parts are obtained with a bottom-up approach (i.e. layer by layer) [5]. However, some "wastes" are always produced since generally a dummy line of 10 – 50 mm is printed (onto the substrate or inside a separate vessel) before each deposition to ensure a homogeneous ink flow, and sometimes printing defects may occur, related to trapped bubbles or impurities present in the paste (**Figure S6**). In this section preliminary studies related to paste reuse are provided aiming to develop a zero-waste process.

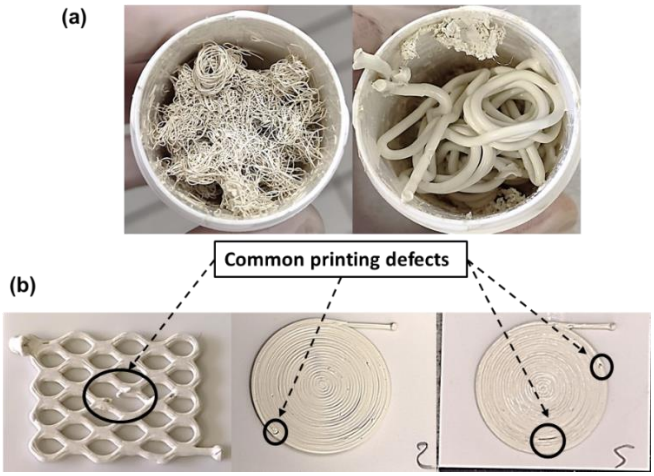

Figure S 6. Examples of 3D-printed scraps produced during extrusion: dummy lines (a) and defected samples (b).

Here, scraps produced during a printing cycle were collected together and amalgamated in the centrifugal planetary mixer imposing 3' mixing at 900 rpm and 3' defoaming at 1200 rpm, and the resulting paste was characterized in terms of thermal and rheological properties. The paste produced from the waste appears very similar to the prepared one (**Figure S7**) in terms of visual appearance, viscosity, and thermal behaviour, therefore it is expected to behave like the freshly prepared paste during 3D printing operations.

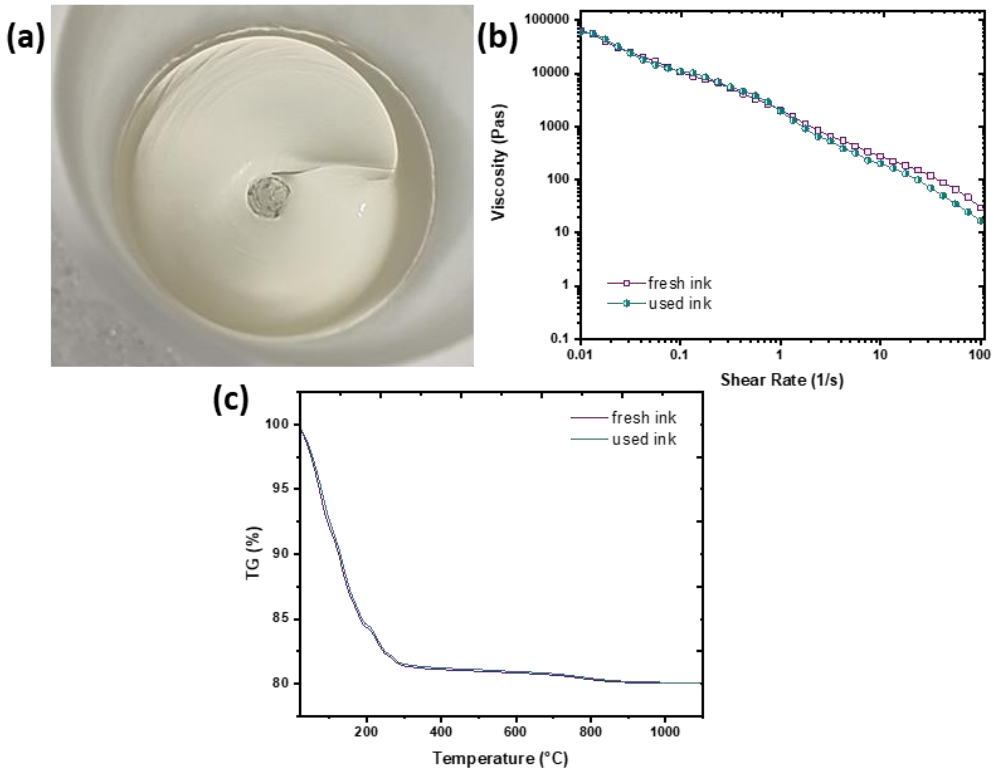

Figure S 7. Macroscopic picture of the reused paste after mixing scraps in the planetary mixer (a), viscosity curve (b), and TG analysis (c) on the fresh and used paste.

Figure S8: Pics of different samples after drying

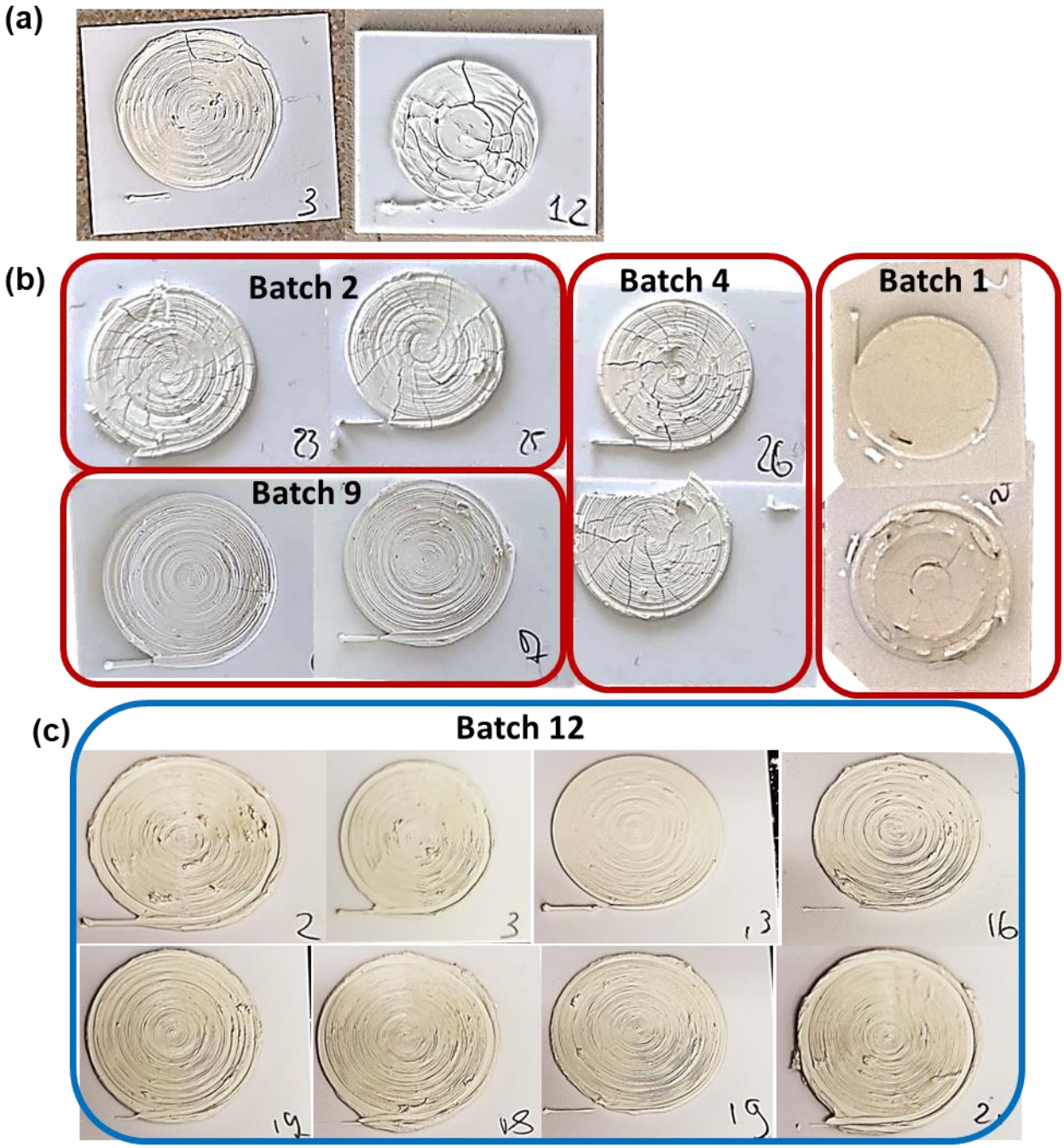

Figure S 8. Pictures of some samples after drying in humidity-controlled chambers (a) and with non-optimized (b) and optimized (c) osmotic drying.

Section S9: Influence of the printing substrate on the lower surface quality of the microextruded parts.

The choice of the printing substrate must be made considering the interaction between the extruded paste and the substrate material and the compatibility with post-printing operations. In the first stage, samples were successfully printed on dense Al_2O_3 plates (0,64 mm thick),

mylar foils (0,20 mm thick) or glass substrates (0,7 mm thick) without shape modification, and no differences were noted between samples extruded on different substrates. However, the high smoothness of glass and mylar causes the samples to detach and move once placed in the PEG bath (**Figure S9**).

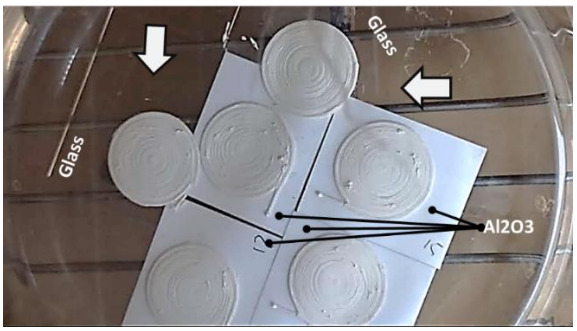

Figure S 9. Macroscopic picture of some samples under osmotic drying printed onto different substrates.

This increases the risk of breaking or damaging the samples during extraction. On the contrary, the use of alumina plates with a certain surface roughness enhances sample adhesion to the substrate, enabling easier handling during all post-printing operations. Furthermore, this surface roughness is negatively reflected on the bottom surface of the printed samples, as shown in **Figure S10**. If some imperfections are present on the substrate, they will also be reflected on the ceramic parts as shown in **Figure S10 e**.

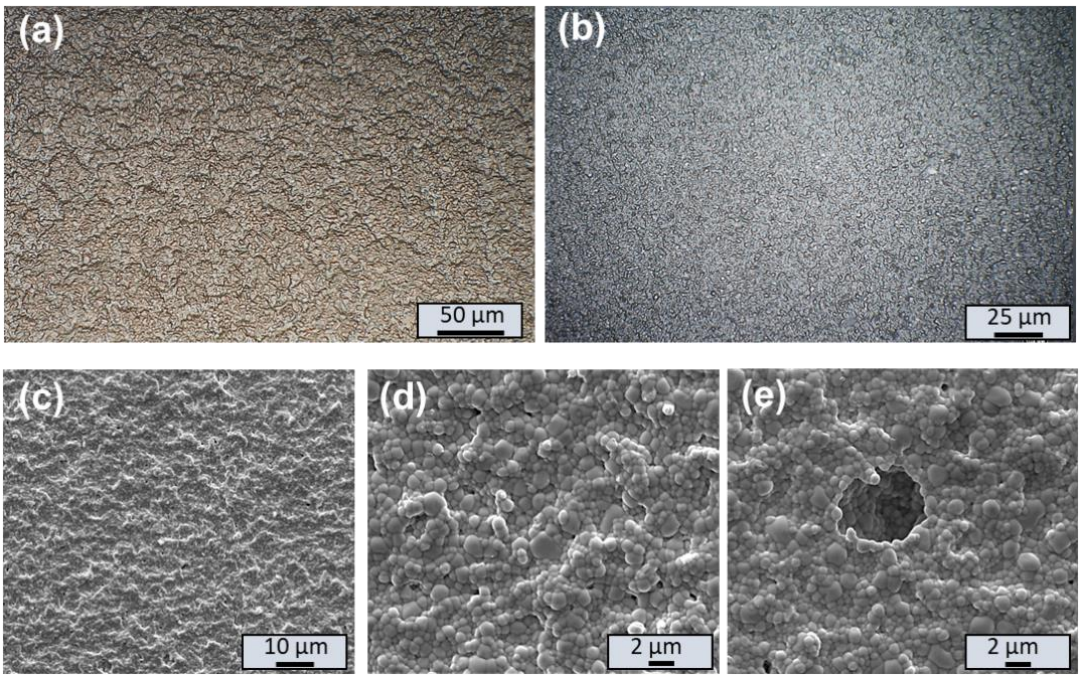

Figure S 10. Optical (a,b) and SEM micrographs with SE detector (c-e) at different magnifications of the lower surface of sintered membranes obtained by microextrusion onto Al_2O_3 plates.

Section S 10: Microstructural characterizations of sintered parts obtained by microextrusion

In this section, more details regarding the microstructure of sintered parts are provided. **Figure S11** displays an in-depth SEM characterization of a bilayer obtained through set-up 2 (i.e. using a 250 µm nozzle size) after thermal treatments. Results show a homogeneous microstructure along the whole cross-section with micrometric-sized grains and pores. No delamination defects can be seen in the contact point between the two stacked layers (i.e. in the middle of the cross-section). As shown in **Figure S12**, also thicker parts composed of two layers printed with the 410 µm nozzle (set up 1) present a homogeneous microstructure with no observable delamination. The elemental EDX mapping of the cross-section is reported in **Figure S13**. The Ba mapping is related to the BCZY phase, while Gd distribution is linked to the GDC phase. Cerium (Ce) is well distributed throughout the cross-section, as it is present in both phases.

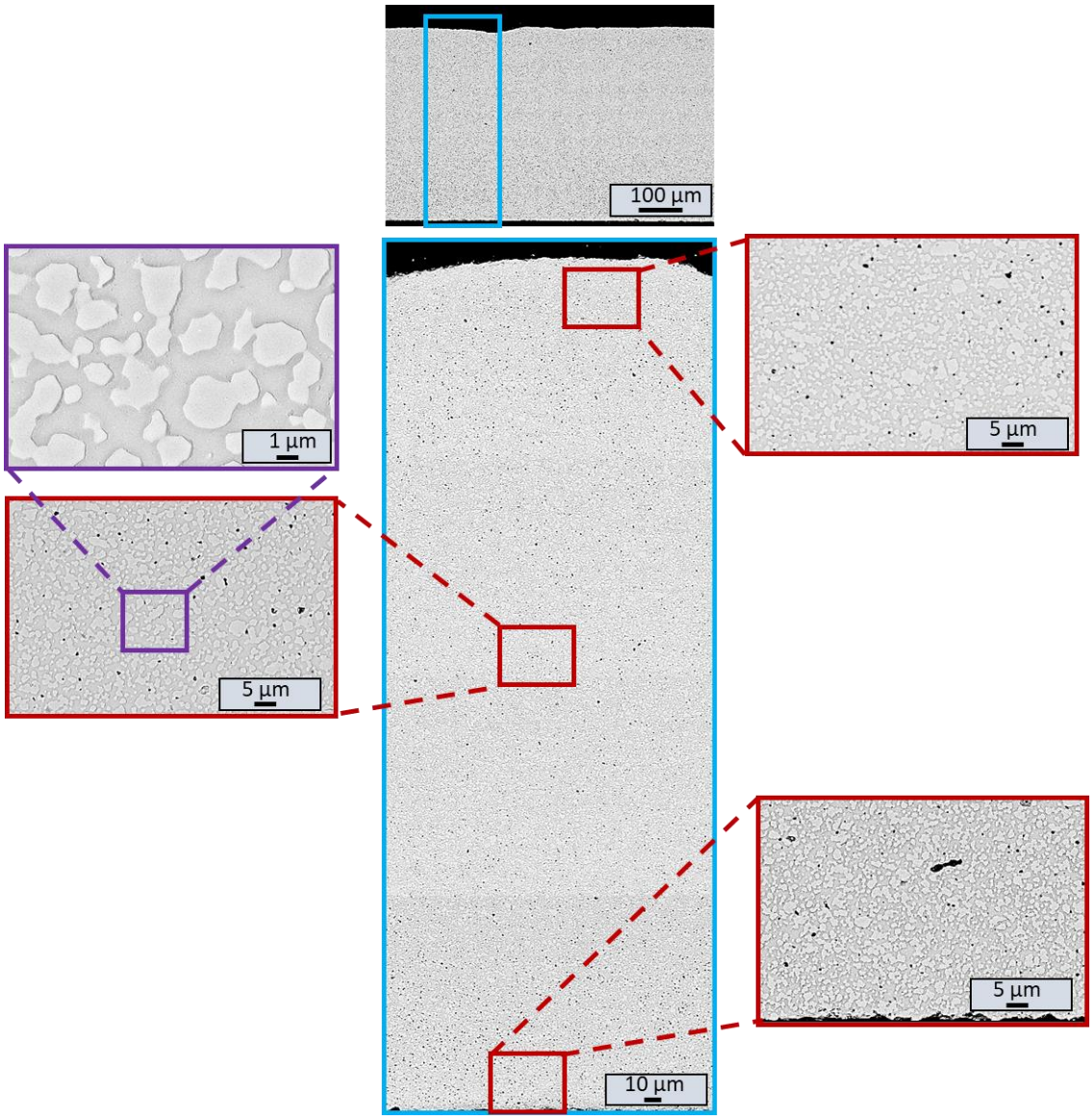

Figure S 11. SEM micrographs with BSE detector of the polished cross section of a sintered bilayer (set up 2, 250 µm nozzle) obtained by microextrusion at different magnifications. Here, lighter grains are associated with the GDC phase, the darker “matrix” is composed of BCZY, and black zones are pores.

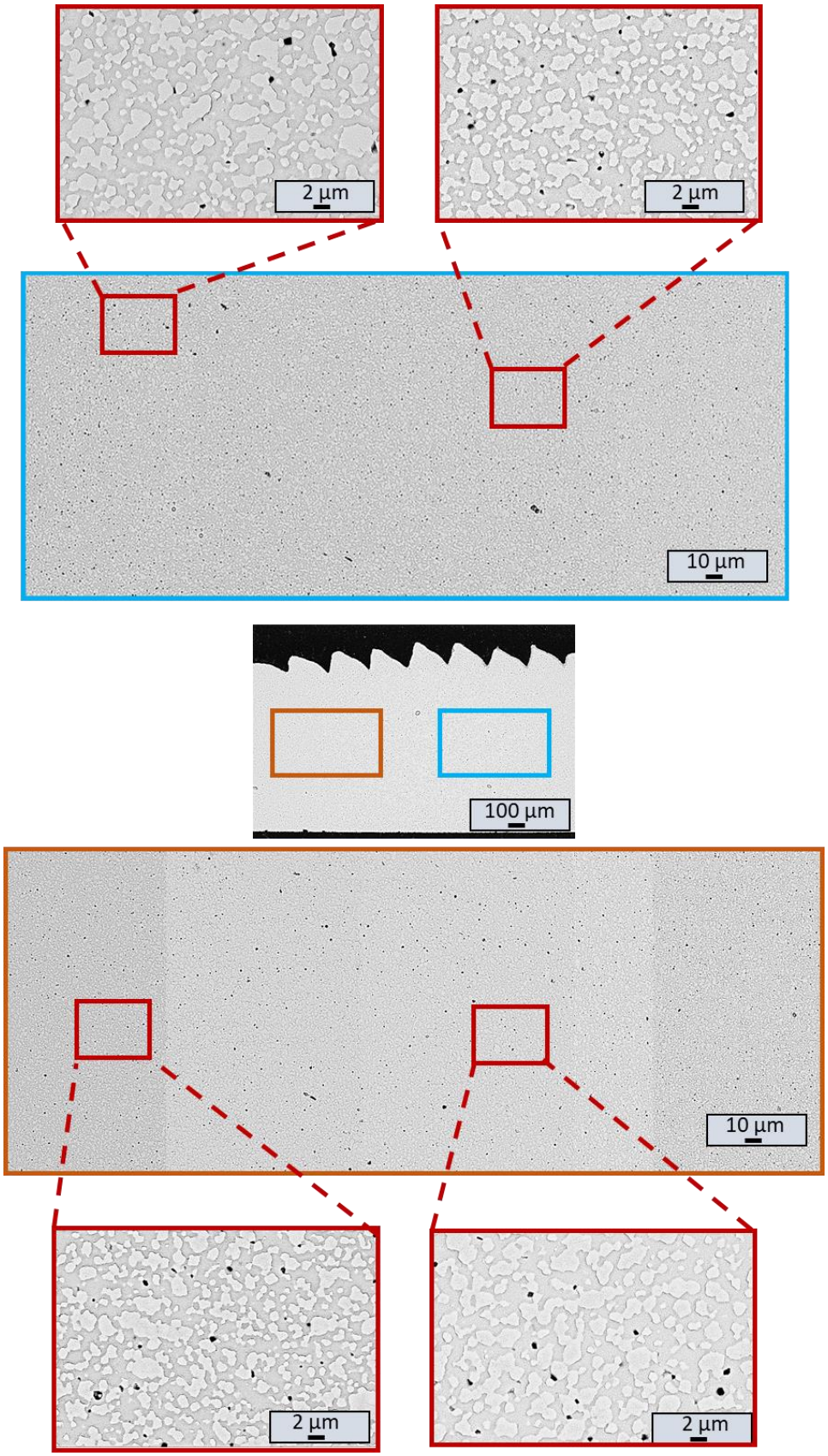

Figure S 12. SEM micrographs with BSE detector of the polished cross section of a sintered bilayer (set up 1, 410 µm nozzle) obtained by microextrusion at different magnifications. Here, lighter grains are associated with the GDC phase, the darker "matrix" is composed of BCZY, and black zones are pores.

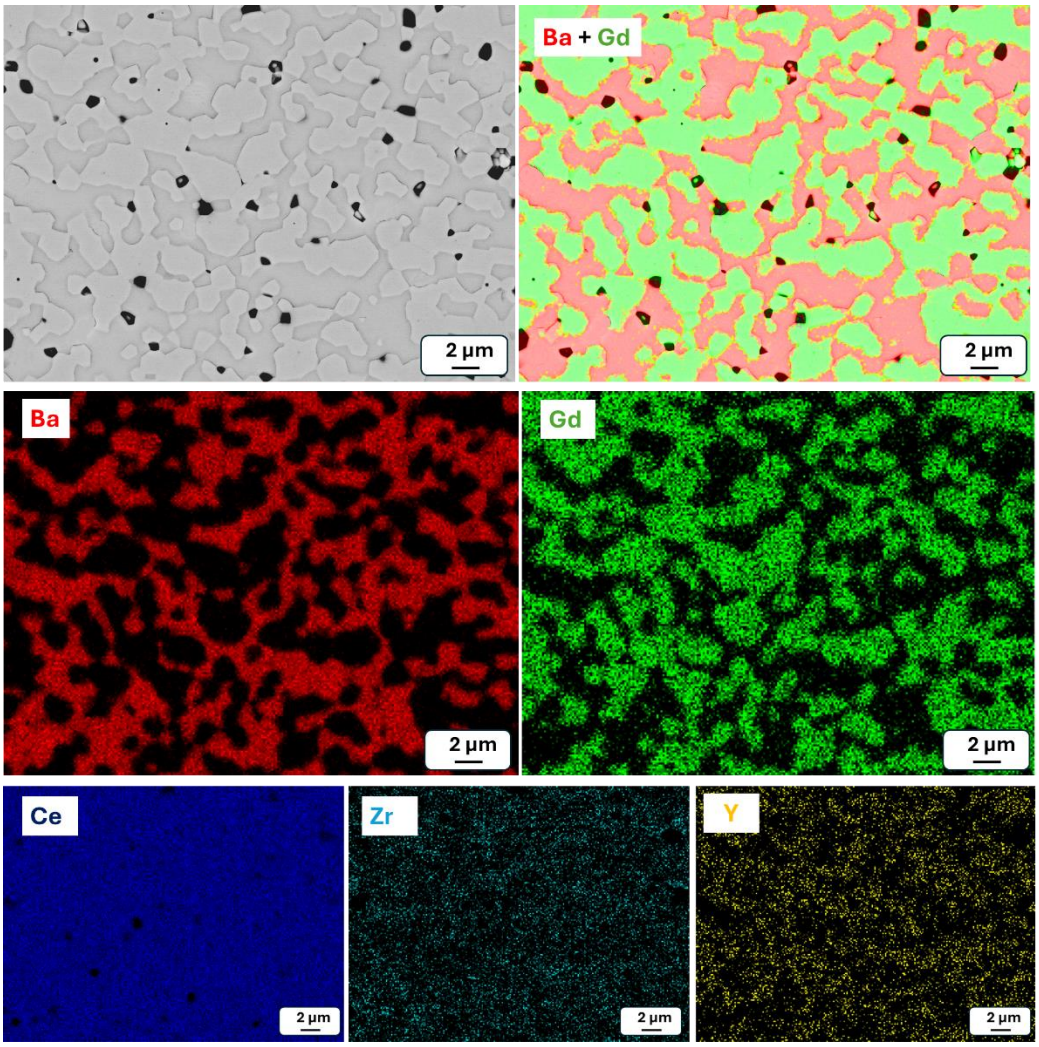

Figure S 13. SEM-EDX maps of a microextruded BCZY-GDC cross-section. The Ba mapping is related to the BCZY phase, while Gd distribution is linked to the GDC phase.

Section S 11: Production of asymmetric structures and test bars by microextrusion

To validate the developed printing methodology (i.e. 3D microextrusion, subsequent osmotic drying with concentrated PEG200 at 60 °C for 110 h, glycol washing in a warm ethanol bath for 5 hours, and thermal treatments) the optimized paste was used also for the production of several samples with different size and geometries.

Grids and honeycomb-type structures

Honeycomb-type and grid porous structures were produced to validate the process with the BCZY-GDC-ZnO paste. The printing parameters employed are shown in **Table S2.**

Table S2. Printing parameters used for the production of porous structures.

Design	Nozzle size (μm)	Q (ml/min)	v (mm/s)	h (mm)	d_{th} (mm)	w (mm)
Honeycomb	410	0.1	5	0.8	0.42	0.40
Grid	250	0.1	10	0.6	0.29	0.39

As shown in **Figure S14**, honeycomb-type specimens were successfully printed with up to six stacked layers. No apparent defects in the external part nor delamination between layers were observed. The open porosity of the scaffold was found to be ≈ 37 %, as measured through image analysis.

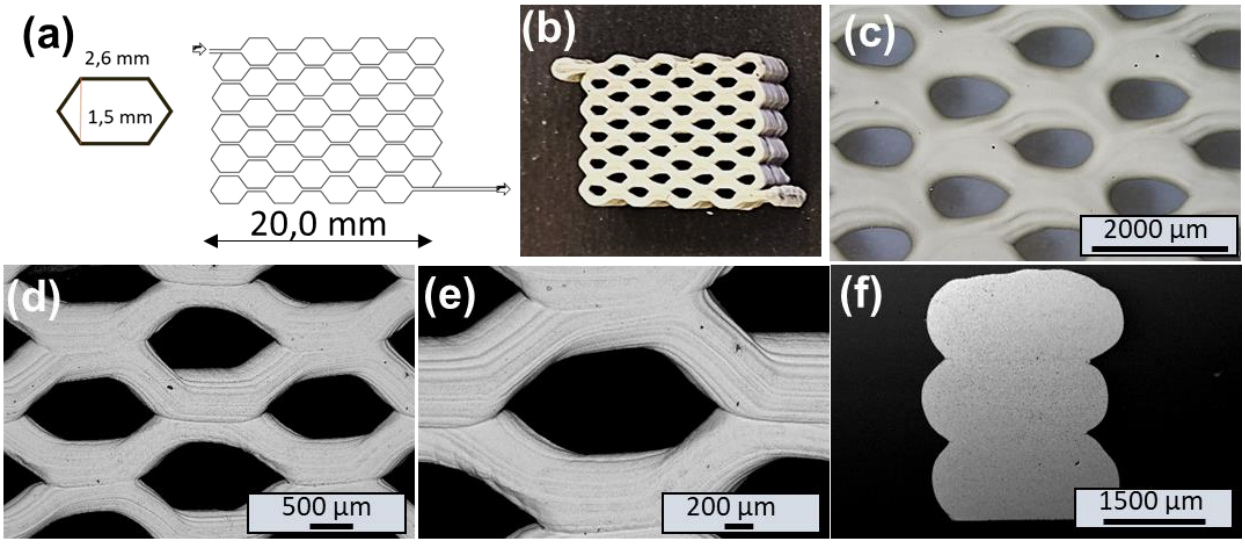

Figure S 14. Sketch of the pattern used to produce honeycomb-type structures (a), picture of a sintered part (b), optical (c) and SEM micrographs of the upper surface (d,e), and a polished cross-section (f) of a tri-layered support.

Flat and defect-free grid-type structures were also produced as shown in **Figure S15**. Here, a 500 μm thick bilayer with ≈ 15 % open porosity (i.e. induced by the design reported in **Figure S15 a**) is reported.

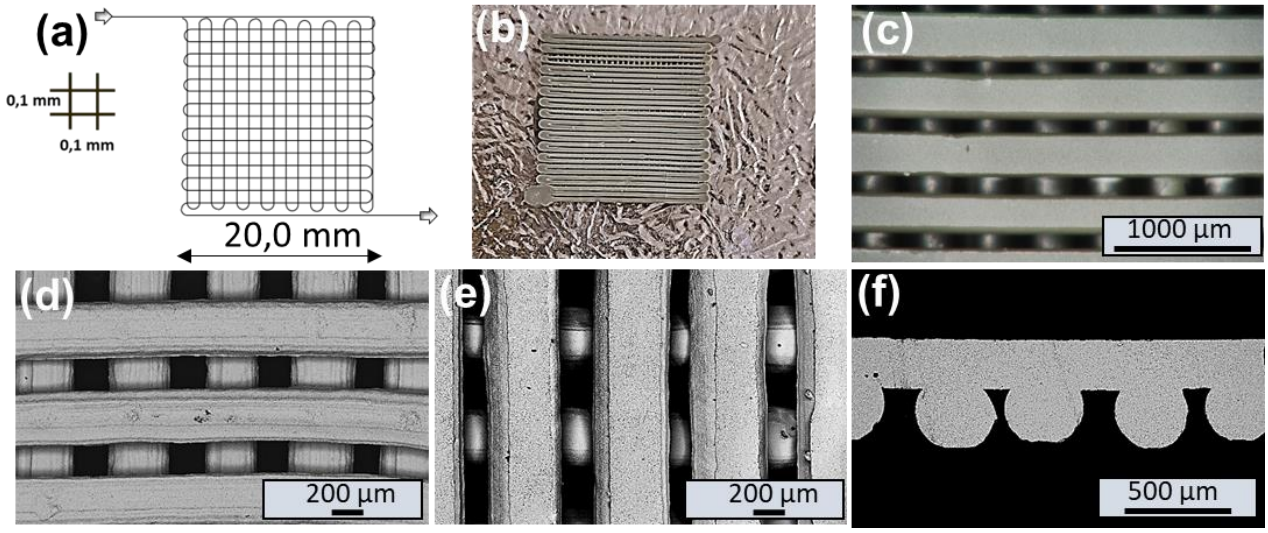

Figure S 15. Sketch of the pattern used to produce grid-type structures (a), picture of a sintered part (b), optical (c) and SEM micrographs of the upper (d) and lower surface (e), and a polished cross section (f) of a bi-layered grid.

Asymmetric structures

An asymmetric architecture is constituted by a thin dense layer supported on a thick porous substrate that provides mechanical strength to the membrane. Asymmetric membranes are generally preferred, for the almost proportional increase in hydrogen permeation with the reduction of the thickness of the active membrane (when permeation across the membrane is controlled by transport through the bulk phase), as postulated by the Wagner equation [6,7].

Asymmetric membranes were produced by printing a circular design onto a squared grid pattern obtained by stacking 2 orthogonal layers. Printing parameters used for the production of both the dense and the porous layer are reported in **Table S3**.

Table S3. Printing parameters used for the production of asymmetric structures.

Function	Design	Nozzle size (µm)	Q (ml/min)	v (mm/s)	h (mm)	d_{th} (mm)	w (mm)
Dense – active layer	**Circular**	250	0.1	10	0.6	0.29	0.15
Porous support	**Grid**	250	0.1	10	0.6	0.29	0.39

As shown in **Figure S16,** planar and crack-free asymmetric membranes were obtained showing dense and support layers of ≈ 250 µm and ≈ 600 µm thick respectively, and a grid

mesh of ≈ 80 x 80 ± 15 µm. A superb contact between the dense and support layers was also observed, as a result of the well-optimized printing parameters.

As mentioned in the main text (*3.2 3D Microextrusion)*, the ink was not able to correctly flow through the 50 µm nozzle (**see Figure S5**), and considering that the typical thickness of the dense layer employed in asymmetric structures is about ≈ 20 µm [8,9], asymmetric membranes were produced as a proof of concept. Further work is still necessary to produce asymmetric structures that can be effectively applied in hydrogen permeation applications.

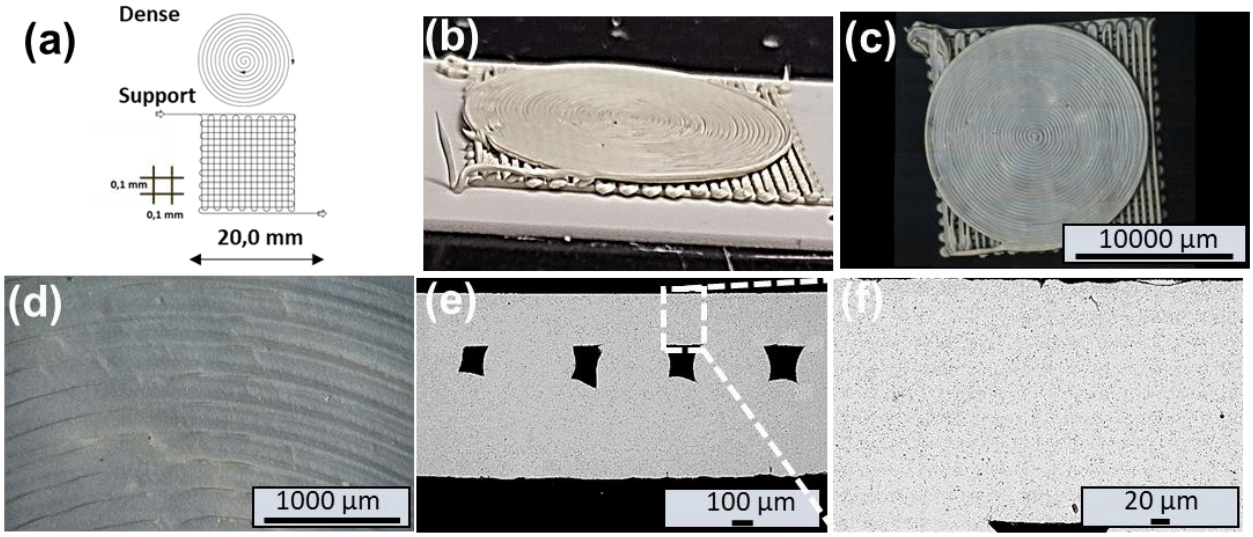

Figure S 16. Schematic representation of the different patterns used to produce asymmetric membranes (a), pic of an as-printed part (b), optical micrographs of a sintered asymmetric membrane (c) and its upper surface (d), SEM micrographs with BSE detector of the polished cross-section at different magnifications (h,i).

Test bars

To evaluate the mechanical strength of 3D printed membranes, some test bars were produced by microextrusion using the printing parameters reported in **Table S4**, with five layers stacked according to the pattern shown in **Figure S17 a**. Similar to the circular membranes produced with the 410 µm nozzle, the lateral and upper parts (**Figure S17 b-d**) present a relatively low surface quality due to the choice of the printing parameter, while the lower surface (**Figure S17 e**) appears flat and smooth. No delamination or defects between layers were observed (**Figure S17 f-h**) indicating the good optimization of the overall process.

Table S4. Printing parameters used for the production of asymmetric structures.

Design	Nozzle size (µm)	Q (ml/min)	v (mm/s)	h (mm)	d_{th} (mm)	w (mm)
Test bars	410	0.1	5	0.55	0.61	0.20

It's worth mentioning that bars were produced in the same manner as the membranes used for hydrogen permeation tests (i.e. printed with the 410 µm nozzle) to ensure accurate validation of their thermomechanical behaviour.

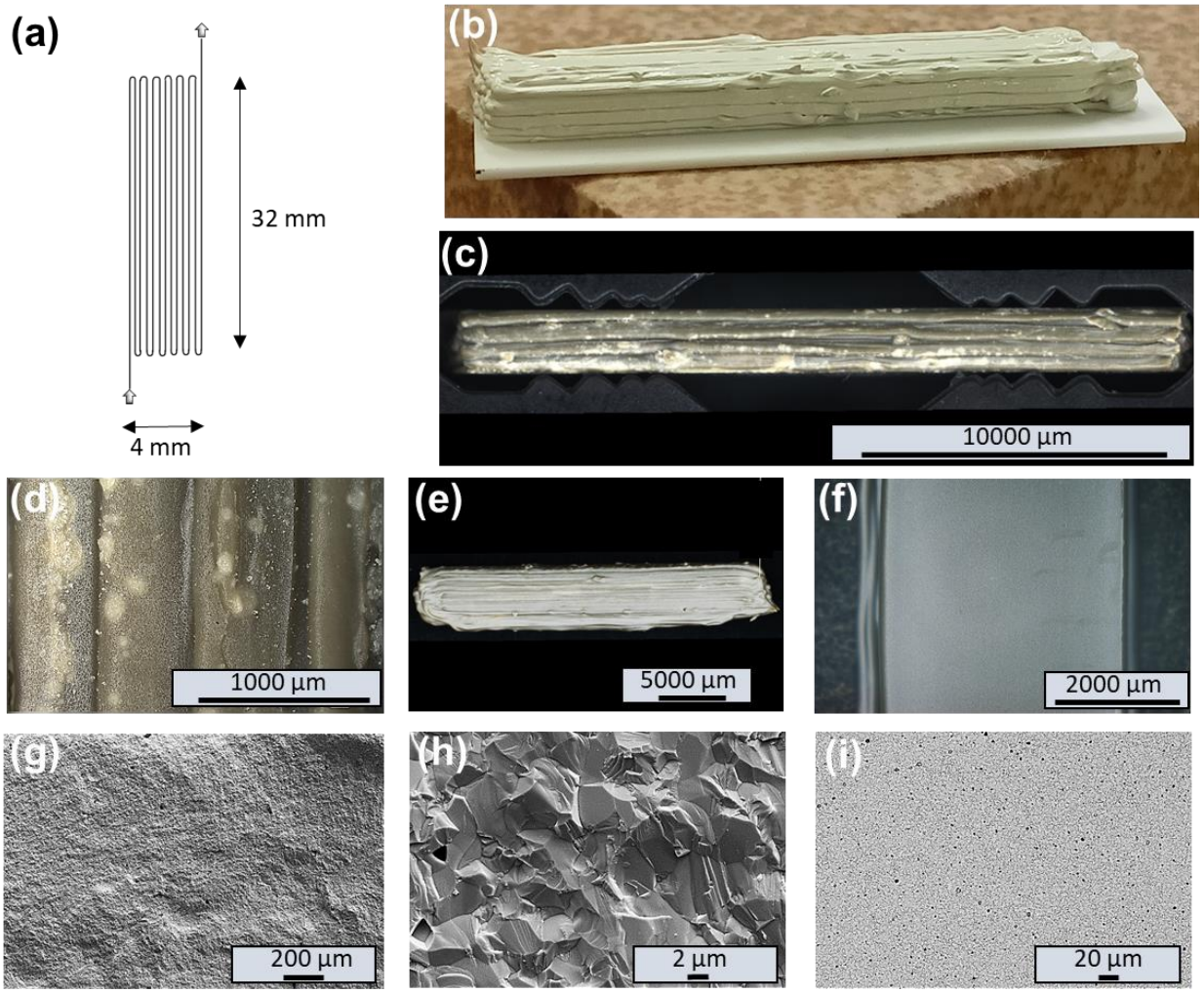

Figure S 17. Schematic representation of the design used to produce test bars (a), pic of an as-printed part (b), optical micrographs of the later (c-d), upper (e) and lower (f) part of a sintered specimen, SEM micrographs of the fracture (g,h) and polished (i) cross-section of a sintered bar produced by microextrusion. Here, lighter grains are associated with the GDC phase, the darker "matrix" is composed of BCZY, and black zones are pores.

Section S12: 4-pt bending tests at 750°C in Ar.

As explained in *Section S11*, test bars obtained by microextrusion present a poor surface quality deriving from the selected printed parameters (**Figure S18 a**), which is unsuitable for mechanical tests. For this reason, specimens were manually machined before testing using sandpaper 500 and SiC grinding paper 1200 (**Figure S18 b**). **Figure S18 c** offers a graphical representation of the results obtained by the 4-point bending tests.

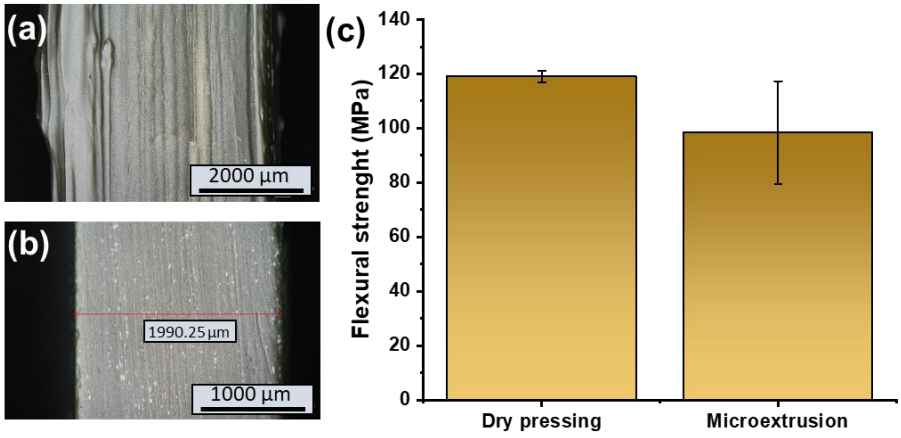

Figure S 18. Optical micrograph of the upper surface of a sintered test bar produced by microextrusion before (a) and after (b) machining; graphical representation of the results obtained from 4-pt bending test at 750°C in Ar (c).

As explained in the main text, understanding the exact failure origin in specimens with higher flexural strength (> 116 MPa) was complicated and sometimes impossible. **Figure S19** shows the fractographic analysis performed on a test bar obtained by dry-pressing, where the failure origin was associated with processing defects such as grinding since the polishing of the test bars was performed manually and no inclusions or abnormal grains were observed [10].

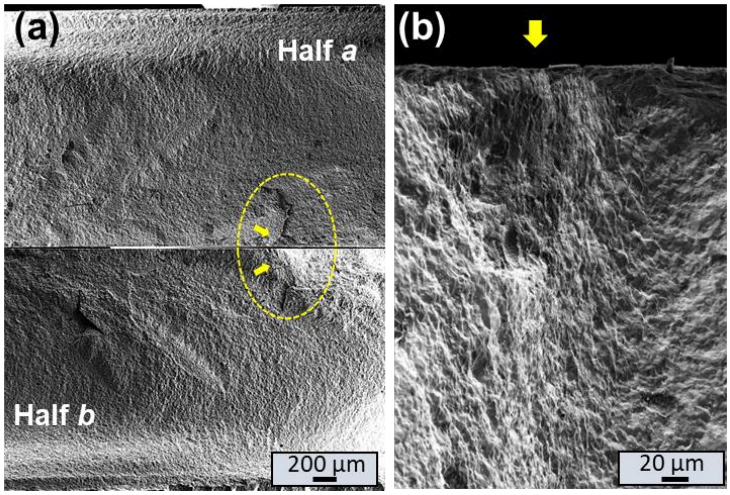

Figure S 19. SEM micrographs of back-to back halves (a) and enlarged view of the failure origin (b) of a test bar produced by dry-pressing after bending test (σ_b = 120 MPa).

Figure S 20: Macroscopic pictures of some membranes used for hydrogen permeation measurements.

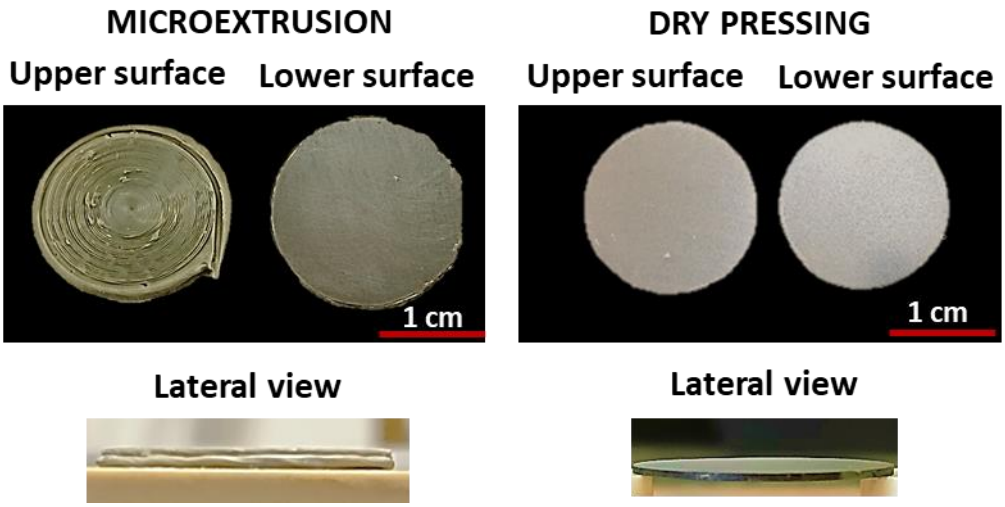

Figure S 20. Pictures of different membranes produced by microextrusion with the 410 µm nozzle and dry-pressing methodology.

REFERENCES

[1] M. Rjeb, A. Labzour, A. Rjeb, S. Sayouri, Y. Claire, A. Périchaud, TG and DSC studies of natural and artificial aging of polypropylene, Physica A: Statistical Mechanics and Its Applications 358 (2005) 212–217. https://doi.org/10.1016/j.physa.2005.06.023.

[2] P. Maitra, J. Ding, H. Huang, S.L. Wunder, Poly(ethylene oxide) Silananted Nanosize Fumed Silica: DSC and TGA Characterization of the Surface, Langmuir 19 (2003) 8994–9004. https://doi.org/10.1021/la034048c.

[3] E. Mercadelli, D. Montaleone, A. Gondolini, P. Pinasco, A. Sanson, Tape-cast asymmetric membranes for hydrogen separation, Ceramics International 43 (2017) 8010–8017. https://doi.org/10.1016/j.ceramint.2017.03.099.
[4] Y. Lakhdar, C. Tuck, J. Binner, A. Terry, R. Goodridge, Additive manufacturing of advanced ceramic materials, Progress in Materials Science 116 (2021) 100736. https://doi.org/10.1016/j.pmatsci.2020.100736.
[5] Z. Liu, Q. Jiang, Y. Zhang, T. Li, H.-C. Zhang, Sustainability of 3D Printing: A Critical Review and Recommendations, in: American Society of Mechanical Engineers Digital Collection, 2016. https://doi.org/10.1115/MSEC2016-8618.
[6] H.J.M. Bouwmeester, A.J. Burggraaf, Dense Ceramic Membranes for Oxygen Separation, in: Handbook of Solid State Electrochemistry, CRC Press, 1997.
[7] J. Garcia-Fayos, J.M. Serra, M.W.J. Luiten-Olieman, W.A. Meulenberg, 8 - Gas separation ceramic membranes, in: O. Guillon (Ed.), Advanced Ceramics for Energy Conversion and Storage, Elsevier, 2020: pp. 321–385. https://doi.org/10.1016/B978-0-08-102726-4.00008-9.
[8] D. Montaleone, E. Mercadelli, S. Escolástico, A. Gondolini, J. M. Serra, A. Sanson, All-ceramic asymmetric membranes with superior hydrogen permeation, Journal of Materials Chemistry A 6 (2018) 15718–15727. https://doi.org/10.1039/C8TA04764B.
[9] A. Gondolini, A. Bartoletti, E. Mercadelli, P. Gramazio, A. Fasolini, F. Basile, A. Sanson, Development and hydrogen permeation of freeze-cast ceramic membrane, Journal of Membrane Science 684 (2023) 121865. https://doi.org/10.1016/j.memsci.2023.121865.
[10] G.D. Quinn, NIST Recommended Practice Guide: Fractography of Ceramics and Glasses, 2nd edition, NIST (2016). https://www.nist.gov/publications/nist-recommended-practice-guide-fractography-ceramics-and-glasses-2nd-edition (accessed August 23, 2024).